The Astrophysical Journal, 660:687–698, 2007 May 1
© 2007. The American Astronomical Society. All rights reserved. Printed in U.S.A.

A NOZZLE ANALYSIS OF SLOW-ACCELERATION SOLUTIONS IN ONE-DIMENSIONAL MODELS OF ROTATING HOT-STAR WINDS

Thomas I. Madura and Stanley P. Owocki
Bartol Research Institute, Department of Physics and Astronomy, University of Delaware, Newark, DE 19716;
tmadura@udel.edu, owocki@bartol.udel.edu

and

Achim Feldmeier
Astrophysik, Institut für Physik, Universität Potsdam, Am Neuen Palais 10, 14469 Potsdam, Germany; afeld@astro.physik.uni-potsdam.de
Received 2006 September 1; accepted 2007 January 8

ABSTRACT

One-dimensional (1D) stellar wind models for hot stars rotating at $\gtrsim$75% of the critical rate show a sudden shift to a slow-acceleration mode, implying a slower, denser equatorial outflow that might be associated with the dense equatorial regions inferred for B[e] supergiants. Here we analyze the steady 1D flow equations for a rotating stellar wind based on a "nozzle" analogy for terms that constrain the local mass flux. For low rotation, we find the nozzle minimum occurs near the stellar surface, allowing a transition to a standard, CAK-type steep-acceleration solution; but for rotations $\gtrsim$75% of the critical rate, this inner nozzle minimum exceeds the global minimum, implying near-surface supercritical solutions would have an overloaded mass-loss rate. In steady, analytic models in which the acceleration is assumed to be monotonically positive, this leads the solution to switch to a slow-acceleration mode. However, time-dependent simulations using a numerical hydrodynamics code show that, for rotation rates 75%–85% of critical, the flow can develop abrupt "kink" transitions from a steep acceleration to a *decelerating* solution. For rotations above 85% of critical, the hydrodynamic simulations confirm the slow acceleration, with the lower flow speed implying densities 5–30 times higher than the polar (or a nonrotating) wind. Still, when gravity darkening and 2D flow effects are accounted for, it seems unlikely that rotationally modified equatorial wind outflows could account for the very large densities inferred for the equatorial regions around B[e] supergiants.

Subject headings: hydrodynamics — stars: early-type — stars: emission-line, Be — stars: mass loss — stars: rotation — stars: winds, outflows

1. INTRODUCTION

Hot, luminous, massive stars of spectral types O and B are generally quite rapid rotators, with inferred surface rotation speeds typically in the range of several hundred kilometers per second, or a substantial fraction of the critical rotation speed (ca. 400–600 km s^{-1}) at which material at the rotating equatorial surface would be in Keplerian orbit. Such luminous stars are also characterized by strong stellar wind outflows, driven by the line scattering of the star's continuum radiation flux (Castor et al. 1975, hereafter CAK). A long-standing question is how such wind outflows are affected by the star's rotation and in particular whether this might play a role in the enhanced equatorial density outflows and/or disks inferred in certain classes of particularly rapid rotators, e.g., Be and B[e] stars.

For classical Be stars, there is now substantial observational evidence (see, e.g., papers in Ignace & Gayley 2005) that the disks are Keplerian in nature, with very limited radial outflow; they are thus probably *not* a direct result of feeding by a steady stellar wind (Owocki 2005). However, for the disk and/or enhanced equatorial outflows inferred in supergiant B[e] stars, wind mechanisms still seem a viable option. For example, Lamers & Pauldrach (1991) and Pelupessy et al. (2000) have noted that the "bistability" enhancement in opacity which occurs for some value of the local surface effective temperature (i.e., for B-type stars at $\sim$22,000 K; see Pauldrach & Puls 1990; Vink et al. 1999) associated with the reduced radiation temperature near the equator can lead to a factor of several enhancement in the radial mass flux. By itself, this seems inadequate to explain equatorial densities estimated to be hundreds or even thousands of times the densities of the polar winds in these stars (Zickgraf et al. 1985; Kraus & Miroshnichenko 2006). However, a recent series of papers by M. Curé and colleagues (Curé 2004; Curé & Rial 2004; Curé et al. 2005) proposes that, for very high, near-critical rotation, a switch of the wind outflow to a slower, shallow-acceleration solution can lead to a further enhancement in density that, together with the bistability effect, might reach the equatorial densities inferred in B[e] supergiants.

This paper aims to understand better the physical origin of these shallow wind acceleration solutions for high rotation rates and to examine critically their likely relevance for explaining dense equatorial disks or outflows.

Modeling rotating, hot-star winds began with the studies by Friend & Abbott (1986, hereafter FA86) and by Pauldrach et al. (1986, hereafter PPK86), who extended the CAK formalism by adding the effect of an outward centrifugal acceleration to one-dimensional (1D) models of the wind outflow in the equatorial plane. Both FA86 and PPK86 independently derived a modified CAK model (mCAK) that relaxes the CAK "point star" approximation and properly accounts for the finite cone angle subtended by the star. They each then found that the reduction in the effective gravity by the outward centrifugal force tends to increase the mass-loss rate and decrease the wind speed. However, for the models computed, up to about 75% of the critical rotation rate, both changes are limited to only a factor of a few and are thus insufficient to produce the large equatorial densities and low velocities inferred in B[e] supergiants. Moreover, for still faster rotation, above about 75% critical, FA86 found that the equations for

outward acceleration could no longer be integrated beyond some finite radius, and thus they were unable to derive any complete flow solutions for such rapid rotation speeds. Subsequent 1D models have investigated the role of magnetic forces (Friend & MacGregor 1984; Poe & Friend 1986) and sound waves (Koninx & Hearn 1992), but as summarized by Bjorkman & Cassinelli (1993) neither mechanism seems favorable for producing slow, dense equatorial outflows.

More fundamentally, the physical relevance of any such 1D models may be limited since accounting for latitudinal flows toward or away from the equator requires at least a two-dimensional (2D) treatment. A vivid example comes from the 2D "wind-compressed disk" (WCD) model of Bjorkman & Cassinelli (1993), which argues that conservation of angular momentum should tend to channel material from higher latitudes toward an equatorially compressed disk flow. If one assumes a purely radial driving force, 2D hydrodynamic simulations (Owocki et al. 1994) confirm the basic WCD effect but show that, depending on whether material reaches the equator above or below some "stagnation point," it either drifts outward or falls back toward the star. Such simultaneous infall-plus-outflow behavior is not possible in a steady 1D model but is a perfectly natural outcome in a 2D simulation. Furthermore, Cranmer & Owocki (1995) showed that, when computed from proper angle integration of intensity from the rotationally distorted stellar surface, the line force also has nonzero, *nonradial* components in both azimuth and latitude. Owocki et al. (1996; see also Petrenz & Puls 2000) showed that such nonradial line forces can *inhibit* the formation of a WCD. Finally, equatorial gravity darkening can actually *reduce* the wind mass flux from the equator and so lead to an equatorial wind density that is *lower*, not higher, than near the poles.

Despite this likely importance of such 2D effects, several recent analyses (Curé 2004; Curé & Rial 2004; Curé et al. 2005) have reexamined the 1D equatorial flow models of FA86, with a particular focus on the failure to obtain monotonically accelerating wind solutions for rotation above about 75% of the critical speed. In particular, these papers argue that for such very high, near-critical rotation, the wind solution can switch to an alternative mode, characterized by a much *slower* outward acceleration. Together with a moderately enhanced mass flux, the resulting lower speed outflow then implies a substantial enhancement in density, relative to the standard CAK, steep acceleration applicable at higher latitudes. When combined with parameterizations intended to mimic a bistability enhancement in the line driving (Lamers & Pauldrach 1991; Pelupessy et al. 2000), Curé et al. (2005) predict equator-to-pole density contrasts of the order of 10^2–10^4.

Assessing the physical relevance of such claims for understanding B[e] stars will eventually require proper account of the multidimensional effects noted above. Nonetheless, to provide a solid basis for such multidimensional models, it is important to have a clearer, dynamical understanding of these novel 1D slow-outflow solutions. By combining analytic studies with numerical hydrodynamic simulations, this paper examines the reality and physical origin of the shallow wind acceleration solutions for high rotation rates, with emphasis on their possible relevance to disk outflows from B[e] supergiants.

We begin (§ 2) with a basic review of the general time-dependent wind equations, together with their CAK-type, steady state solutions in a nonrotating wind. To provide a physical basis for extending these steady models to include rotation, we first (§ 3) apply a simple "nozzle" analysis (see Holzer 1977; Abbott 1980), originally developed to study winds driven from luminous accretion disks (Pereyra et al. 2004). With a few judicious, yet quite reasonable, approximations (e.g., neglecting gas pressure terms by taking the zero sound-speed limit, using a beta velocity law to evaluate the finite-disk correction as an explicit function of radius), it is possible to obtain simple integrations of the equation of motion and to study the scalings of the mass-loss rate with rotation, as well as the switch from steep- to shallow-acceleration solutions beyond a threshold rotation rate. To test the validity of these simple analytic solutions, we next apply a numerical hydrodynamics code (§ 4) to evolve 1D rotating wind models to asymptotic steady states (§ 5.1). Results confirm a transition to slower acceleration at very high rotation (above about 85% of critical) but also show a new class of nonmonotonic "kink" solutions that apply for moderately fast rotation (ca. 75%–85% of critical). We then examine (§§ 5.2–5.3) the time evolution of solutions in various rotation domains, with emphasis on the kink solutions and on a peculiar transition case (85% of critical rotation), characterized by an initial wind overloading followed by a flow stagnation and eventual reaccretion of material onto the star. We conclude with a summary and outlook for future work (§ 6).

2. GENERAL FORMALISM FOR LINE-DRIVEN MASS LOSS

2.1. *1D Time-dependent Equations of Motion*

In this paper, we examine 1D radiatively driven outflow in the equatorial plane of a rotating star. For the general time-dependent simulations discussed in § 3, the relevant equations for conservation of mass and radial component of momentum have the form

$$\frac{\partial \rho}{\partial t} + \frac{1}{r^2}\frac{\partial (r^2 \rho v)}{\partial r} = 0, \tag{1}$$

$$\frac{\partial v}{\partial t} + v\frac{\partial v}{\partial r} = \frac{v_\phi^2}{r} - \frac{1}{\rho}\frac{\partial P}{\partial r} - \frac{GM_*(1-\Gamma_e)}{r^2} + g_{\rm lines}, \tag{2}$$

where r and t are the radius and time, and ρ and v are the mass density and radial component of the velocity. The body forces here include the outward radiative acceleration from line scattering, $g_{\rm lines}$, and an effective inward gravitational acceleration, $GM_*(1-\Gamma_e)/r^2$, reduced by the outward continuum radiative force from scattering by free electrons, as accounted for by the Eddington parameter, $\Gamma_e = \kappa_e L_*/4\pi GM_* c$. For the centrifugal term, v_ϕ^2/r, we avoid explicit treatment of an azimuthal momentum equation by assuming simple angular momentum conservation (which is a good approximation in the supersonic flow domain considered here), yielding then for the azimuthal speed

$$v_\phi = v_{\rm rot}\frac{R_*}{r}, \tag{3}$$

where $v_{\rm rot}$ is the rotation speed at the star's equatorial surface radius R_*. For simplicity, we also avoid a detailed treatment of the wind energy balance by assuming an isothermal outflow, for which the pressure is written as $P = \rho a^2$, where a is the (constant, isothermal) sound speed.

2.2. *Steady State Equations with Rotation*

For the simplified case of a steady state, the time-dependent terms vanish ($\partial/\partial t = 0$), yielding for the steady acceleration

$$v\frac{dv}{dr} = -\frac{GM_*(1-\Gamma_e)}{r^2} + \frac{v_{\rm rot}^2 R_*^2}{r^3} + g_{\rm lines} - \frac{a^2}{\rho}\frac{d\rho}{dr}. \tag{4}$$

The steady form for mass conservation implies a constancy for the overall mass-loss rate, $\dot{M} \equiv 4\pi\rho v r^2$. Using this to eliminate the density ρ, the equation of motion (4) takes the form

$$\left[1 - \frac{a^2}{v^2}\right] v \frac{dv}{dr} = -\frac{GM_*(1-\Gamma_e)}{r^2} + \frac{v_{\rm rot}^2 R_*^2}{r^3} + g_{\rm lines} + \frac{2a^2}{r}. \quad (5)$$

The factor in square brackets on the left-hand side allows for a smooth mapping of the wind base onto a hydrostatic atmosphere below the sonic point, where $v < a$. However, in radiatively driven winds the pressure terms on the right-hand side are generally negligible since, compared to the gravitational acceleration term that must be overcome to drive a wind, these are of order $w_s \equiv (a/v_{\rm esc})^2 \approx 0.001$, where $v_{\rm esc} \equiv [2GM_*(1-\Gamma_e)/R_*]^{1/2}$ is the effective escape speed from the stellar surface radius R_*.

Since the key to a stellar wind is overcoming gravity, it is convenient to define a dimensionless equation of motion that scales all accelerations by the effective gravity,

$$\left(1 - \frac{w_s}{w}\right) w' = -1 + \omega^2(1-x) + \Gamma_{\rm lines} + \frac{4w_s}{1-x}, \quad (6)$$

where $\Gamma_{\rm lines} \equiv g_{\rm lines} r^2/GM_*(1-\Gamma_e)$, and the gravitationally scaled inertia is $w' \equiv dw/dx = r^2 v(dv/dr)/GM_*(1-\Gamma_e)$. The independent variable here is the inverse radius coordinate $x \equiv 1 - R_*/r$, while the dependent variable is the ratio of the radial kinetic energy to the effective surface escape energy, $w \equiv v^2/v_{\rm esc}^2$. Gas pressure effects are accounted for by terms containing $w_s \equiv a^2/v_{\rm esc}^2$, while centrifugal effects from rotation are characterized in terms of the ratio of the equatorial rotation speed to critical speed, $\omega \equiv v_{\rm rot}/v_{\rm crit} = \sqrt{2} v_{\rm rot}/v_{\rm esc}$, under the assumption that the wind material conserves its surface value of specific angular momentum, $r v_\phi(r) = v_{\rm rot} R_*$.

Within the CAK formalism for driving by scattering of a point source of radiation by an ensemble of lines, the deshadowing of optically thick lines by the Doppler shift associated with the wind acceleration gives the scaled radiative acceleration $\Gamma_{\rm lines}$ a power-law dependence on the flow acceleration w',

$$\Gamma_{\rm lines} = C w'^{\alpha}, \quad (7)$$

where α is the CAK power index. Here we have eliminated an inverse dependence on density ρ in favor of the mass-loss rate $\dot{M} = 4\pi r^2 \rho v$, with the line force constant thus defined by

$$C \equiv \frac{1}{1-\alpha}\left(\frac{L_*}{\dot{M}c^2}\right)^{\alpha}\left(\frac{\bar{Q}\Gamma_e}{1-\Gamma_e}\right)^{1-\alpha}, \quad (8)$$

with L_* the stellar luminosity and Γ_e the Eddington parameter for the gravitationally scaled radiative acceleration from electron scattering opacity, κ_e (in square centimeters per gram; Lamers & Cassinelli 1999; Owocki 2004). We have also used the Gayley (1995) $\bar{Q}$ notation for the overall normalization of the line opacity. Note that, for fixed sets of stellar parameters (L_*, M_*, Γ_e) and line opacity $(\alpha, \bar{Q})$, the constant C scales with the mass-loss rate as $C \propto 1/\dot{M}^{\alpha}$.

As already noted, the smallness of the dimensionless sound-speed parameter w_s implies that gas pressure plays little role in the dynamics of any line-driven stellar wind. Hence, to a good approximation, we can obtain accurate solutions by analyzing the much simpler limit of vanishing sound speed $a \propto w_s^{1/2} \rightarrow 0$, for which the line-driven wind equation of motion reduces to

$$w' = -1 + \omega^2(1-x) + C w'^{\alpha}. \quad (9)$$

2.3. *Classical CAK Solution for a Point Star*

Let us first review the standard CAK solution without rotation, setting $\omega = 0$. Note then that since the parameters Γ_e and C are spatially constant, the solution is independent of radius. For high $\dot{M}$ and small C there are no solutions, while for small $\dot{M}$ and high C there are two solutions. The CAK *critical* solution (denoted by the subscript c) corresponds to a *maximal* mass-loss rate, which requires a *tangential* intersection between the line force $C w'^{\alpha}$ and the combined inertia plus gravity $1 + w'$, for which

$$\alpha C_c w_c'^{\alpha-1} = 1, \quad (10)$$

and thus, together with the equation of motion (9), we have

$$w_c' = \frac{\alpha}{1-\alpha}, \quad (11)$$

with

$$C_c = \frac{1}{\alpha^{\alpha}(1-\alpha)^{1-\alpha}}. \quad (12)$$

Using equation (8), this then yields the standard CAK scaling for the mass-loss rate,

$$\dot{M}_{\rm CAK} = \frac{L_*}{c^2}\frac{\alpha}{1-\alpha}\left(\frac{\bar{Q}\Gamma_e}{1-\Gamma_e}\right)^{(1-\alpha)/\alpha}. \quad (13)$$

Moreover, since the scaled equation of motion (9) has no explicit spatial dependence, the scaled critical acceleration w_c' applies throughout the wind. This can therefore be trivially integrated to yield

$$w(x) = w(1)x, \quad (14)$$

where $w(1) = \alpha/(1-\alpha)$ is the terminal value of the scaled flow energy. In terms of dimensional quantities, this represents a specific case of the general beta velocity law,

$$v(r) = v_\infty\left(1 - \frac{R_*}{r}\right)^{\beta}, \quad (15)$$

where in this case $\beta = \frac{1}{2}$, and the wind terminal speed scales with the effective escape speed from the stellar surface, $v_\infty = v_{\rm esc}[\alpha/(1-\alpha)]^{1/2}$.

2.4. *Finite-Disk Form for the CAK Line Force*

The above analysis is based on the idealization of radially streaming radiation, as if the star were a point source at the origin. This was the basis of the original CAK wind solutions, although they did already identify (but did not implement) the appropriate "finite-disk correction factor" (FDCF) to account for the full angular extent of the star (see Castor et al. 1975, eq. [50]),

$$f(r) = \frac{(1+\sigma)^{1+\alpha} - \left(1+\sigma\mu_*^2\right)^{1+\alpha}}{(1+\alpha)\sigma(1+\sigma)^{\alpha}\left(1-\mu_*^2\right)}, \quad (16)$$

with $\mu_* \equiv (1 - R_*^2/r^2)^{1/2}$ the cosine of the finite cone angle of the stellar disk and $\sigma \equiv d\ln v/d\ln r - 1$. When this factor is included to modify the point-star CAK line acceleration (from eq. [7]), its complex dependence on radius, velocity, and velocity gradient complicates the solution of the full equation of motion. Full solutions derived independently by FA86 and PPK86 yield a

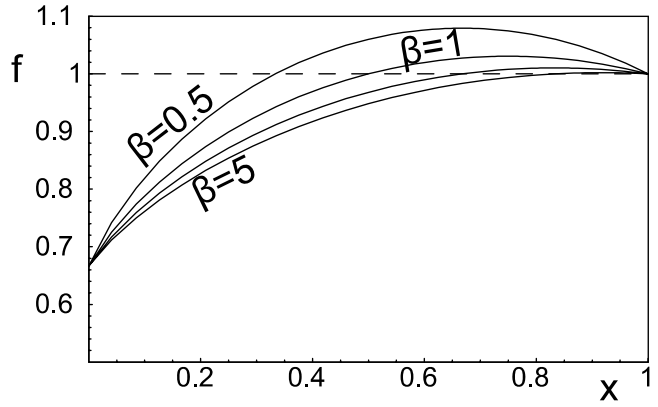

FIG. 1.—Spatial variation of the FDCF f vs. scaled inverse radius $x = 1 - R_*/r$ for CAK exponent $\alpha = \frac{1}{2}$ and various velocity-law exponents, $\beta = 0.5, 1, 2$, and 5. The horizontal dashed line denotes the unit correction that applies at the point of isotropic expansion (where $\sigma = d \ln v/d \ln r - 1 = 0$) and at large distances where the star approaches the point-source form assumed in the original CAK model.

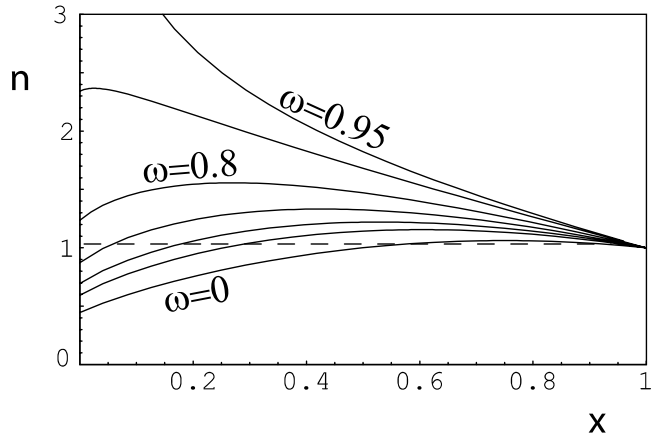

FIG. 2.—Nozzle function $n(x)$ vs. scaled inverse radius $x = 1 - R_*/r$ for various rotation rates $\omega = 0, 0.5, 0.6, 0.7, 0.8, 0.9$, and 0.95, ranging from lowermost to uppermost. All curves use a $\beta = 1$ velocity law in evaluating the FDCF. The horizontal dashed line at unit value represents the nozzle function for the CAK point-star model, with $n = f = g = 1$.

somewhat reduced mass-loss rate $\dot{M}_{\rm fd} \approx \dot{M}_{\rm CAK}/(1+\alpha)^{1/\alpha}$ and higher terminal speed $v_\infty \approx 3v_{\rm esc}$.

But if we approximate the wind velocity law by the simple beta-law form of equation (15), then the FDCF can be evaluated as an *explicit* spatial function. Figure 1 illustrates the resulting variation of f with the scaled coordinate x for $\alpha = \frac{1}{2}$ and various values of β. Note that the overall form is quite similar for all cases, increasing from a surface value $f_* \equiv f(R_*) = 1/(1+\alpha)$ to past unity at the isotropic expansion radius (where $dv/dr = v/r$), $r/R_* = (1+\beta)$ [corresponding to $x = \beta/(1+\beta)$], and eventually returning asymptotically to unity from above at large radii ($x \to 1$).

In the steady wind analysis in the next section, we thus choose the canonical value $\beta = 1$ to represent the FDCF as an explicit spatial function (PPK86).

3. STEADY STATE SOLUTIONS FOR 1D MODELS OF ROTATING, LINE-DRIVEN STELLAR WINDS

3.1. *Nozzle Analysis for Steady Wind Acceleration*

Let us now examine how the combined effects of the FDCF and rotation alter the classical CAK result. Note that we are ignoring here gravity darkening and oblateness effects, as well as any bistability in the line-driving parameters between the polar and equatorial wind. For a rotating star and wind, the FDCF can become even more complicated, modified by the rotational shear of the wind outflow and by the oblateness of the star, and possibly also by the equatorial gravity darkening of the source radiation (Cranmer & Owocki 1995; Gayley & Owocki 2000). However, for simplicity, let us nonetheless base our analysis on the spatially explicit form obtained by assuming a canonical $\beta = 1$ velocity law (15) within finite-disk factor (16) for a simple spherical expansion. In the zero sound-speed limit, the scaled equation of motion (9) can now be written in the form

$$w' = -1 + \omega^2(1-x) + f C_c \left(\frac{w'}{\dot{m}}\right)^{\alpha}, \qquad (17)$$

where we have normalized the line force in terms related to the point star CAK model, with $\dot{m} \equiv \dot{M}/\dot{M}_{\rm CAK}$, the ratio of the mass-loss rate to the point-star CAK value. Note then that for the nonrotating ($\omega = 0$), point-star ($f = 1$) case of the classical CAK model, the critical solution (with maximal mass loss) is given by $\dot{m} = 1$ and $w(x) = \alpha/(1-\alpha)x$. As noted in § 2.3, this implies a CAK mass-loss rate $\dot{M} = \dot{M}_{\rm CAK}$ and a velocity law $v(r) = v_\infty(1 - R_*/r)^{1/2}$, with terminal speed $v_\infty = [\alpha/(1-\alpha)]^{1/2} v_{\rm esc}$.

To analyze models with rotation, a particularly convenient case is to take $\alpha = \frac{1}{2}$, for which the equation of motion (17) (using eq. [12] for C_c) becomes a simple quadratic in $(w')^{1/2}$,

$$w' - 2f\sqrt{\frac{w'}{\dot{m}}} + g(x) = 0, \qquad (18)$$

where for convenience we have defined a rotationally reduced gravity as $g(x) \equiv 1 - \omega^2(1-x)$. We can then solve for a shallow ($-$) and steep ($+$) acceleration solution,

$$w'_\pm(x) = \frac{g(x)n(x)}{\dot{m}}\left[1 \pm \sqrt{1 - \frac{\dot{m}}{n(x)}}\right]^2, \qquad (19)$$

with the "nozzle function,"

$$n(x) \equiv \frac{f(x)^2}{g(x)} = \frac{f(x)^2}{1 - \omega^2(1-x)}. \qquad (20)$$

The significance of this nozzle function stems from its appearance with the mass-loss rate $\dot{m}$ within the square-root discriminant (cf. de Laval nozzle; Abbott 1980). In particular, we can readily see that maintaining a numerically real flow acceleration requires[1] a mass-loss rate $\dot{m} \le \min[n(x)]$. As such, the location of the global minimum of this function (the smallest nozzle "throat") represents the *critical point* that sets the maximal allowed value of the mass-loss rate, $\dot{m} = \min[n(x)]$, that is consistent with a monotonically accelerating outflow.

Figure 2 plots $n(x)$ versus x for various rotation rates ω, using a $\beta = 1$ velocity law to obtain a spatially explicit approximation to the FDCF. Note that for no or low rotation (about $\omega < 0.75$), the minimum of the nozzle function is less than unity and occurs at the stellar surface, $x = 0$. This allows the flow to transition to a

[1] Actually, this restriction really stems from our CAK scaling of the line force with w'^{α} [in this case $(w')^{1/2}$], which requires a strictly *positive* acceleration, $w' > 0$. But if we provide a backup scaling for negative accelerations, then "overloaded" situations, for which the square-root discriminant in eq. (19) becomes negative, simply lead to an abrupt switch, a so-called kink (Cranmer & Owocki 1996), to a *decelerating* solution. See §§ 4 and 6 for further details.

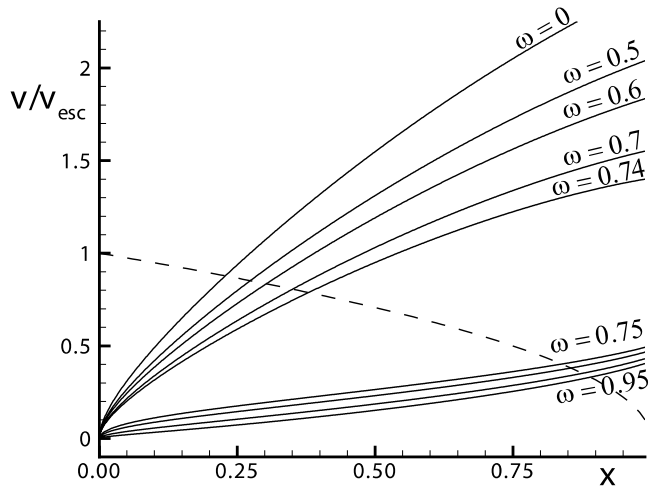

FIG. 3*a*

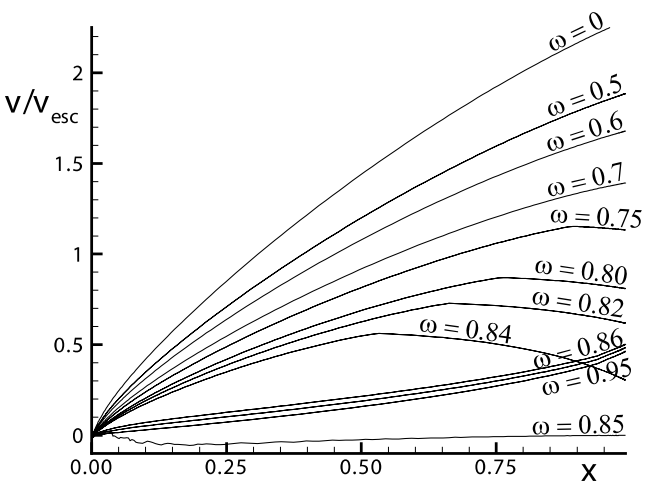

FIG. 3*b*

FIG. 3.—(*a*) Flow speed over escape speed, $v/v_{\rm esc} = w^{1/2}$, vs. scaled inverse radius $x = 1 - R_*/r$, as derived from a nozzle analysis, using a steep acceleration for no or modest rotation, $\omega = 0$, 0.5, 0.6, 0.7, and 0.74 and shallow acceleration for rapid, near-critical rotation, $\omega = 0.75$, 0.8, 0.85, 0.9, and 0.95. The dashed curve shows the escape speed as a function of x. (*b*) Same as (*a*), but as found using asymptotic states of full hydrodynamic simulations. Note again the steep, supercritical accelerations for no or modest rotation, $\omega = 0$, 0.5, and 0.7, and shallow, subcritical accelerations for rapid, near-critical rotation, $\omega = 0.86$, 0.9, and 0.95. However, note also the kink solutions present for $\omega = 0.75$, 0.8, 0.82, and 0.84 and the collapsed solution for $\omega = 0.85$.

supercritical outflow directly from the static surface boundary condition $w(0) = 0$, following the steeper, plus (+) root for the acceleration in equation (19), but with a mass-loss rate less than the point-star CAK value,

$$\dot{m} = \dot{m}_0 \equiv n(x = 0) \equiv \frac{f^2(x = 0)}{1 - \omega^2} = \frac{4/9}{1 - \omega^2}. \qquad (21)$$

Note that the factor of 4/9 in the numerator is just the $\alpha = \frac{1}{2}$ value for the zero-rotation, finite-disk corrected mass loss scaling derived by FA86 and PPK86,

$$\dot{m}_{\rm fd} \equiv \frac{\dot{M}_{\rm fd}}{\dot{M}_{\rm CAK}} = f_*^{1/\alpha} = \frac{1}{(1 + \alpha)^{1/\alpha}}. \qquad (22)$$

By contrast, for large rotation rates (about $\omega > 0.75$), this nozzle minimum is unity and occurs at large radii, $x = 1$; satisfying the static surface boundary condition now implies that the flow at all finite radii should remain *subcritical*, following the shallower, minus (−) root for the acceleration in equation (19), now with a mass-loss rate just equal to the point-star CAK value, $\dot{m} = 1$.

This thus provides the basic explanation for the switch from steep to shallow accelerations inferred by Curé et al. (2005).

3.2. *Nozzle Solutions for the Velocity Law in 1D Rotating Winds*

The associated wind velocity laws can be obtained by simple numerical integration of equation (19) from a static boundary $w(0) = 0$, following either the steep or the shallow solution, depending on whether the rotation rate is high enough to shift the critical point [where $n(x)$ has its absolute minimum] from the surface ($x = 0$) to large radii ($x = 1$). Figure 3*a* plots the resulting velocity laws for selected slow versus rapid rotation rates, yielding the steep versus shallow types of flow solution, respectively. The dashed curve in Figure 3*a* plots the escape speed $v_{\rm esc}$ as a function of x, showing that these winds are capable of escaping the star. Figure 3*b* compares results from full dynamical simulations described below.

Figure 4 illustrates the associated terminal speed and mass-loss rates for these solutions (*solid lines*), plotted as a function of rotation rate ω. As the rotation increases past the threshold rate at $\omega \approx 0.75$, the solid curves show an abrupt shift from steep acceleration to shallow acceleration, with the mass loss saturating to the point-star CAK value, $\dot{m} = 1$. The dashed curves show extrapolated results if the local nozzle minimum at the surface is instead used to set flow conditions; the mass loss in this case is set by the scaling $\dot{m}_0$ in equation (21), and the terminal speed is derived by assuming a pure gravitational coasting for all radii

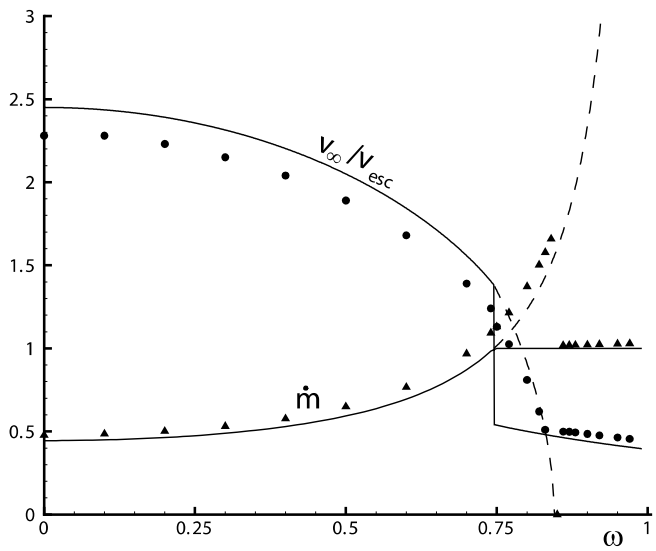

FIG. 4.—*Upper solid curve*: Terminal flow speed over escape speed, $v_\infty/v_{\rm esc} = [w(1)]^{1/2}$, vs. rotation rate ω, showing the shift from fast to slow wind as rotation rate is increased past ca. $\omega = 0.75$. *Lower solid curve*: Mass-loss rate in units of point-star CAK value vs. rotation rate ω, showing the saturation at the CAK mass-loss rate for rapid rotation, $\omega > 0.75$. Dashed curves show the continued steady decrease in $v_\infty/v_{\rm esc}$ and increase in $\dot{m}$ if the local nozzle minimum at the stellar surface is used to set flow conditions (§ 3.2). The circles ($v_\infty/v_{\rm esc}$) and triangles ($\dot{m}$) show corresponding results from full hydrodynamic simulations.

with $n(x) < \dot{m}_0$. The data points again compare corresponding results for the full dynamical simulation, as described further in the next sections.

4. SPECIFICATIONS FOR NUMERICAL HYDRODYNAMICS SIMULATIONS

The above nozzle analysis provides a helpful framework for understanding the nature of flow solutions from a rotating wind model but is based on some key simplifications, e.g., neglect of gas pressure (inclusion of which would lead to a wind that is not supercritical directly from the static surface boundary) and an approximate, spatially explicit form for the FDCF. Moreover, it implicitly assumes that the derived solutions are the only relevant stable, attracting steady states for the rotating wind outflow. To test the validity of these simplifications and assumptions, let us now examine the *time* evolution of analogous 1D flow models, also including both the finite gas pressure and the dynamically computed FDCF. Our specific approach here is to use a numerical hydrodynamics code to evolve a 1D time-dependent model of the equatorial plane for a line-driven stellar wind from a rotating star toward an equilibrium steady state for the resulting flow. The results of these simulations can then be compared to those predicted by the steady state nozzle analysis presented above.

The numerical models presented here were computed using a piecewise parabolic method (PPM; Collela & Woodward 1984) hydrodynamics code called VH-1, originally developed at the University of Virginia (J. Blondin). The basic code was modified for the present study to include radiative driving terms, solving the time-dependent equations for 1D spherical outflow equations (1) and (2). The spatial mesh uses $n_r = 600$ radial zones extending from the base at the stellar surface, $r_1 = R_{\rm min} = R_*$, to a maximum $r_{600} = R_{\rm max} = 100R_*$, with the zone spacing starting at $\Delta r_1 = 6.18 \times 10^{-5} R_*$ and then increasing by 2.5% per zone out to $r_{350} = 15R_*$, after which it remains constant at $\Delta r = 0.333R_*$ to the outer boundary. Tests with double the grid resolution for selected cases give similar results to the above standard values.

The parabolic method requires flow variables to be specified in a phantom zone beyond each boundary. At the outer radius, we assume supercritical outflow, with boundary conditions set by simple flow *extrapolation* assuming constant gradients. This is justified because, as discussed in the Appendix, when finite sound-speed terms are included, the critical point for even the shallow-acceleration solutions should be well within our assumed outer boundary radius of $R_{\rm max} = 100R_*$.

At the inner boundary, the velocity in the two radial zones below $i_{\rm min}$ is set by constant-slope extrapolation, thus allowing the base velocity to adjust to whatever is appropriate for the overlying flow (Owocki et al. 1994). This usually corresponds to a subsonic wind outflow, although inflow at up to the sound speed is also allowed. The base density is fixed at $\rho_0 = 8.709 \times 10^{-13}$ g cm^{-3}, a value chosen because, for the characteristic wind mass fluxes of these models, it yields a steady base outflow that is moderately subsonic. A lower boundary density much smaller than this produces a base outflow that is supersonic and thus is unable to adjust properly to the mass flux appropriate to the overlying line-driven wind. On the other hand, a much larger base density makes the lower boundary too "stiff," leading to persistent oscillations in the base velocity (Owocki et al. 1994).

These time-dependent simulations also require setting an *initial condition* for the density and velocity over the entire spacial mesh at some starting time $t = 0$. For this we generally use a standard, finite-disk corrected CAK wind, computed by relaxing a 1D, *nonrotating* simulation to a steady state; however, for selected models with moderately rapid rotation, we also explore using a slow-acceleration initial condition (see § 5.3). From the assumed initial condition, the models are advanced forward in time steps set to a fixed fraction 0.25 of the Courant time.

Our version of VH-1 is set up to operate in cgs units, requiring specification of physical values for the basic parameters for both the star (e.g., mass, radius, and luminosity) and wind (e.g., CAK k, α, and δ). Building on our earlier studies of Be stars, the specific parameters chosen here are for a main-sequence B star with mass $M_* = 7.5\ M_\odot$, radius $R_* = 4\ R_\odot$, luminosity $L_* = 2310\ L_\odot$, and temperature $T = 2 \times 10^4$ K; but we have also explored models with parameters appropriate for supergiant B[e] stars. These stellar parameters imply an Eddington parameter of $\Gamma_e = 0.008$, an isothermal sound speed of $a = 16.6$ km s^{-1}, and escape and critical speeds of $v_{\rm esc} = 845$ km s^{-1} and $v_{\rm crit} = 597$ km s^{-1}. We also assume a CAK power-law index of $\alpha = \frac{1}{2}$ and cumulative line-strength parameter $\bar{Q} = 1533$ (Gayley 1995). The value of δ has been set to zero in all simulations.

In any case, for a given choice of the CAK power-law index α, we find that results are largely independent of the specific physical parameters when cast in appropriately scaled units, normalizing, for example, radius by the stellar radius R_*, velocity by the wind terminal velocity v_∞ (which in turn scales with the stellar surface escape speed), time by the characteristic flow time R_*/v_∞, and mass-loss rate in terms of the classical (point star) CAK value given in equation (13). To facilitate comparison with the analytic nozzle analysis in §§ 2 and 3, we again choose $\alpha = \frac{1}{2}$ and plot all simulation results using the above scalings.

We further note that essentially all the key VH-1 results reported here were very well reproduced by a completely independent, simple dimensionless hydrodynamics code developed by one of us (A. F.; Feldmeier & Nikutta 2006). Finally, in such time-dependent simulations of line-driven winds, one must also supply a generalized scaling for the line force that applies in the case of nonmonotonic flow acceleration. In general this requires taking into account *nonlocal* couplings of the line transfer (see, e.g., Feldmeier & Nikutta 2006), but we wish here to retain the substantial advantages of using a purely local form for the line driving. Noting that a negative velocity gradient implies a prior line resonance that shadows radial photons from the star, a lower limit would be just to set $g_{\rm line} = 0$ whenever $dv/dr < 0$. On the other hand, since forward scattering can substantially weaken any such shadowing by a prior resonance, an upper limit would be to compute the local line force using the absolute value of the velocity gradient, $g_{\rm line} \propto |dv/dr|^\alpha$. As a simple compromise between these two extremes, we choose here a scaling that truncates the radial velocity gradient to zero whenever it is negative, i.e., $dv/dr \rightarrow \max(dv/dr, 0)$. For a point-star model with radially streaming radiation, this would give a zero line force (since $dv/dr < 0$), but when one accounts for the lateral expansion v/r within the FDCF, it leads to a line force in which the usual dependence on radial velocity gradient is replaced by a dependence on the expansion gradient,

$$g_{\rm line} \propto \left(\frac{v}{r}\right)^\alpha . \tag{23}$$

This leads to a line acceleration that is intermediate between the underestimate and overestimate of the two more extreme scalings.

5. COMPARISON WITH TIME-DEPENDENT HYDRODYNAMIC SIMULATIONS

5.1. *Asymptotic Steady States of Time-dependent Simulations*

In our basic parameter study, each simulation is run using the same initial condition, spatial mesh, boundary conditions, base

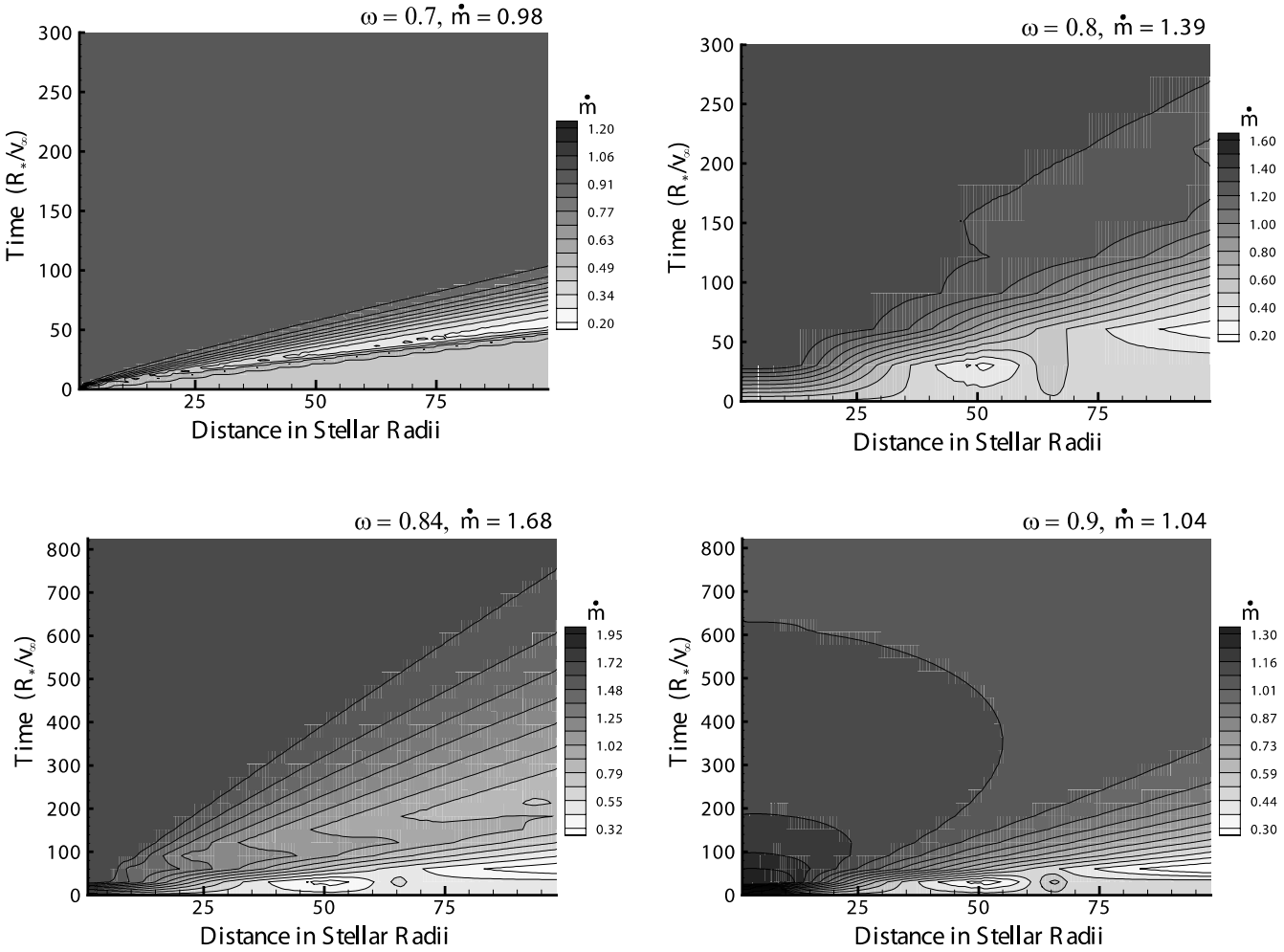

FIG. 5.—Gray-scale plots showing time evolution of mass-loss rate in units of the point-star CAK value. The corresponding rotation rate and final mass-loss rate are given above each plot. Time is in units of the flow time $t = R_*/v_\infty$. Note in each the eventual constancy of the mass-loss rate with both radius and time, indicating relaxation to a steady state solution. Note that the ranges for both gray scale and time differ for each panel.

density, etc., with the only variation being the rotation rate ω, which is set to specific values ranging from 0.1 to 0.97. With only one exception (for the $\omega = 0.85$ case, which turns to be a rather pathological value; see § 5.2), all simulations asymptotically relax to a well-defined steady state. Moreover, for both moderate rotation ($\omega < 0.75$) and high rotation ($\omega > 0.85$), these asymptotic states agree remarkably well with the predictions of the above nozzle analysis. Figure 3*b* shows the velocity laws for these final states, scaled in the same form used in Figure 3*a* for the nozzle-analysis results. Note that both Figures 3*a* and 3*b* show a steep acceleration for no or modest rotation ($\omega = 0$–0.7) and shallow acceleration for rapid, near-critical rotation ($\omega = 0.86$, 0.9, and 0.95).

However, for the moderately high rotation rate cases $\omega = 0.75$, 0.8, 0.82, and 0.84, note also the appearance of a new class of *kink* solutions, characterized by an abrupt shift to a decelerating or "coasting" flow beyond a well-defined "kink radius" $r_{\rm kink}$. These kink solutions thus represent a kind of intermediary final state of the time-dependent simulations in the parameter ranges $0.75 < \omega < 0.85$, effectively smoothing the abrupt jump from fast- to slow-acceleration solutions expected from steady state analyses. The formation of such kinks and their underlying physical cause are discussed further in the section below (§ 5.2) on time evolution.

Figure 4 shows that the fully dynamical results for the scaled ratio of right boundary speed (*circles*) and CAK-scaled mass-loss rate (*triangles*) are generally in good agreement with the predictions of the simple nozzle analysis (*solid curves*), with the modest, ca. 10% differences likely attributable to inclusion in the simulations of a small but finite sound speed (Owocki and ud-Doula 2004). However, for rotation rates $0.75 < \omega < 0.85$, the dynamical results tend to follow the dashed curves of the extended nozzle analysis, representing extended fast solutions, rather than the abrupt shift to slow solutions, indicated by the solid curves. As discussed above, this range of rotation rates is characterized by kink solutions. To understand better this development of fast versus slow versus kink solutions, let us now examine the time evolution of the simulations toward asymptotic states.

5.2. *Time Relaxation of 1D Rotation Models*

For the specific rotation rates $\omega = 0.7$, 0.8, 0.84, and 0.90, which span the parameter range between fast- and slow-acceleration solutions, Figure 5 uses gray-scale plots of the mass-loss rate (in units of the point-star CAK value) to illustrate the time relaxation from the CAK initial condition (set to a nonrotating, finite-disk corrected CAK model) to an asymptotic steady state. Time is given in units of the flow time $t = R_*/v_\infty$, and the final values of the scaled mass-loss rate are indicated above the associated plot. Note that there are distinct differences in the time evolution of each model, with the more rapid rotation cases characterized by a longer relaxation time, but the temporal and spatial constancy of

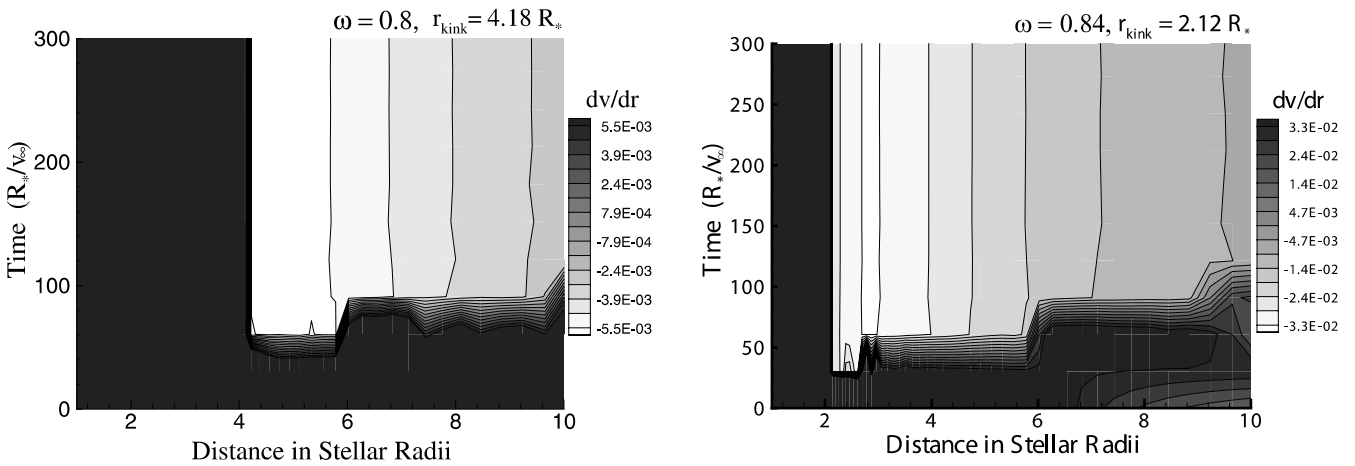

FIG. 6.—Gray-scale plots showing time evolution of the scaled velocity gradient in cgs units. The corresponding rotation rate and kink location $r_{\rm kink}$ are given above each plot.

the final mass-loss rates illustrate the steady nature of the asymptotic solutions.

Despite this temporal and radial constancy in the mass flux, the asymptotic states of the models with $\omega = 0.8$ and 0.84 include a kink, or abrupt discontinuity in their velocity gradient. To illustrate the formation of these kinks, the gray scales in Figure 6 show the evolution of the scaled velocity gradient. In both cases, the abrupt switch from a steep-acceleration solution to a decelerating solution is apparent from the sharp transition from positive to negative velocity gradient, with the kink radius, $r_{\rm kink}$, indicated above each plot. Since, despite the radial discontinuity, the velocity gradient contours all become constant in time, we see clearly that the kink solutions are indeed perfectly valid steady states.

Note, however, that the kink radius shifts from $r_{\rm kink} = 4.18R_*$ for the $\omega = 0.8$ model to $r_{\rm kink} = 2.12R_*$ for the more rapid rotation, $\omega = 0.84$ model. From the velocity-law plots in Figure 3*b*, this also implies that the more rapid rotating case has a more extended deceleration region and thus ends up with a much lower final speed. We can thus anticipate that a somewhat faster rotation rate should give an even lower kink radius, with the more extended decelerating region leading to an even lower final speed, or perhaps even to a flow stagnation (zero velocity) at a finite radius. In particular, note from Figure 4 that the dashed extrapolation curve suggests that the onset of such flow stagnation should occur near a rotation rate of $\omega \approx 0.85$.

In fact, our numerical simulations do show that models near this rate have a quite pathological behavior. This is illustrated in Figure 7, which presents gray-scale plots of the time evolution for the mass-loss rate (Fig. 7*a*) and the scaled velocity gradient (Fig. 7*a*) in this $\omega = 0.85$ case. An overloading of the wind and eventual collapse of the time-dependent solution are shown in these figures. In the first 300 flow times, there is an initial kink formation, but at its lower radius of $r_{\rm kink} = 1.77R_*$ the kink outflow speed is quite low, $v_{\rm kink} \approx 370$ km s^{-1}, well below the local escape speed $v_{\rm esc}(r_{\rm kink}) \approx 640$ km s^{-1}. With the reduced line driving in the decelerating region, the wind outflow now *stagnates* at a finite radius, $r_{\rm stag} \approx 10R_*$. There material accumulates until it is eventually pulled back by the stellar gravity into a reaccretion onto the star, effectively quenching both the kink and base outflow.

For this particular case, the outflow never fully recovers from this quenching, but for only slightly more rapid rotation, $\omega \gtrsim 0.86$, any flow stagnation occurs relatively close to the star, with a

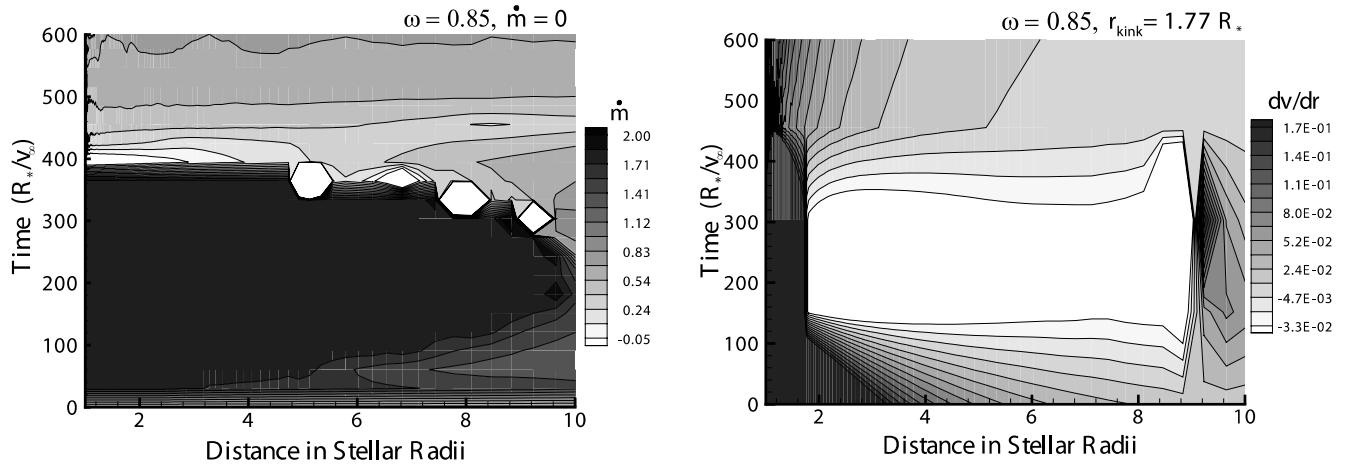

FIG. 7*a* FIG. 7*b*

FIG. 7.—(*a*) Gray-scale plot of the local mass-loss rate in units of the point-star CAK value for $\omega = 0.85$, showing the collapse of the solution. Note the pileup of material at a distance of $r \approx 10R_*$ and the eventual stagnation of the wind and reaccretion of material back onto the stellar surface. (*b*) Gray-scale plot of the scaled velocity gradient in cgs units for $\omega = 0.85$. In the time interval between $t = 150$ and 300 flow times, a kink in the velocity gradient is clearly visible, with the kink location at $r_{\rm kink} \approx 1.77R_*$. After $t \approx 300$, this kink solution becomes overloaded and unstable, eventually collapsing.

TABLE 1
COMPARISON OF KINK LOCATIONS

ω	$r_{\rm kink,\,hydro}$ (R_*)	$r_{\rm kink,\,nozzle}$ (R_*)
0.80.....	4.18	4.54
0.82.....	2.95	3.03
0.83.....	2.52	2.54
0.84.....	2.12	2.16
0.85.....	1.77	1.86

NOTE.—The quantities $r_{\rm kink,\,hydro}$ and $r_{\rm kink,\,nozzle}$ are the kink locations found from numerical hydrodynamic models and from the semianalytic nozzle analysis, respectively.

correspondingly faster and less massive reaccretion, followed by a recovery to a *slow*-acceleration solution, as indicated in Figures 3 and 4. In the very rapid, near-critical rotation case $\omega = 0.90$, no kink or flow stagnation forms, and the solution relaxes more directly to the slow solution, as illustrated in the bottom right panel of Figure 5.

Finally, Table 1 compares the radius of the kinks found in our numerical simulations with the radius at which the nozzle analysis indicates a steep-acceleration solution can no longer be maintained. For cases in which the mass flux set at the base $\dot{m} = \dot{m}_0 = n(x = 0)$ is above the CAK value, i.e., $\dot{m} = n(x = 0) > 1$, this occurs at a radius x_k where a declining nozzle function falls back to $n(x_k) = \dot{m}$. The corresponding radius $r_{\rm kink,\,nozzle}$ agrees quite well with the kink locations found from the hydrodynamic simulations, $r_{\rm kink,\,hydro}$. Note also that the requirement $n(x = 0) = (4/9)/(1 - \omega^2) > 1$ implies rotation rates of $\omega > \sqrt{5}/3 \approx 0.745$, representing the onset for either possible kink solutions or a switch to a slow-acceleration solution.

5.3. *Results for Slow-Acceleration Initial Condition*

A central finding of the dynamical simulations is that moderately fast rotation models $0.75 < \omega < 0.85$ form fast-acceleration kink solutions instead of the slow-acceleration solutions predicted from steady state analyses. But since the nonlinear character of the flow equations allows more than one solution, this raises the question of whether slow-acceleration solutions in this regime might also be stable attractors, perhaps for initial conditions that are closer to their slower outflow form than the fast, nonrotating model used for the initial conditions in the simulation models discussed above. For each of the specific rotation cases in this transitional range, $\omega = 0.75$, 0.80, 0.82, and 0.84, we thus recompute simulations that instead use an initial condition set to the slow-acceleration steady state found for the faster, near-critical rotation case $\omega = 0.9$.

For the $\omega = 0.75$ case, we find that the model again relaxes to a fast solution with an outer-wind kink at $r_{\rm kink} \approx 10R_*$. Steep-acceleration solutions are also recovered in all the slower rotation models as well.

However, as shown in Figure 8, for the $\omega = 0.80$, 0.82, and 0.84 cases the final states now do approach slow-acceleration solutions, apart from a persistent peculiar upward kink near the outer boundary (i.e., for $x > 0.9$ in Fig. 8). Such models also show persistent small-scale fluctuations with an amplitude of ca. 10% in the mass flux, apparently reflecting some difficulty for the numerical solution to relax to a subcritical flow solution in these cases. The upward kink may stem from using a supercritical outflow boundary condition for this slow-acceleration solution, which does not become supercritical until far from the star.

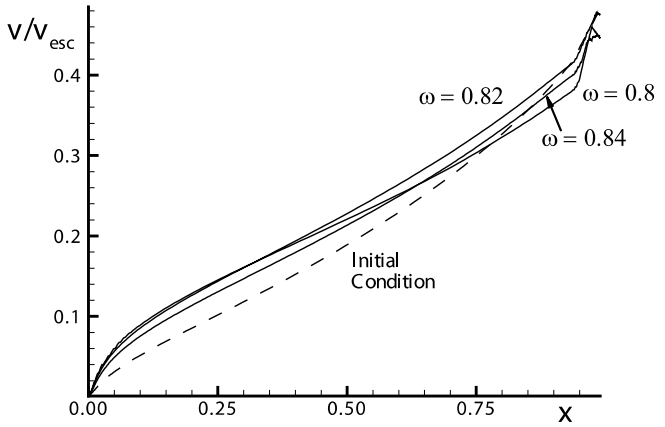

FIG. 8.—Final wind velocity law (flow speed over escape speed, $v/v_{\rm esc}$, vs. scaled inverse radius x) for $\omega = 0.8$, 0.82, and 0.84 simulations that used the $\omega = 0.9$ final state (*dashed line*) as an initial condition. The solid lines now approximate the expected slow-acceleration solution, except for an unexplained uptick in velocity gradient near the right boundary, $x > 0.9$.

Finally, even for this slow-acceleration initial condition, the peculiar case $\omega = 0.85$ still forms an overloaded condition with flow stagnation and reaccretion, after which it never fully recovers a steady outflow result.

5.4. *1D Results for Equatorial Density*

These results also allow us to identify the radial variation of the relative density enhancement in the slow equatorial wind of a rotating star, compared to the nonrotating solution that applies to the polar wind. Here we are ignoring gravity darkening and oblateness effects, as well as any bistability in the line-driving parameters between the polar and equatorial wind. From the analysis of § 3, the relative density enhancements are given by the ratios of the quantity $\dot{m}/w^{1/2}$ between the rotating and nonrotating models.

The dashed curves in Figure 9 show the spatial variation of this density enhancement for rotating models with $\omega = 0.8$, 0.86, 0.9, and 0.95. Note that the enhancements are a few factors of 10, not insignificant but not sufficient to reproduce the inferred densities of B[e] disks, which are factors of the order of 10^4 or more denser than a typical polar wind outflow (Zickgraf et al. 1985; Kraus & Miroshnichenko 2006). Inclusion of bistability effects could give about another factor of a few by increasing the

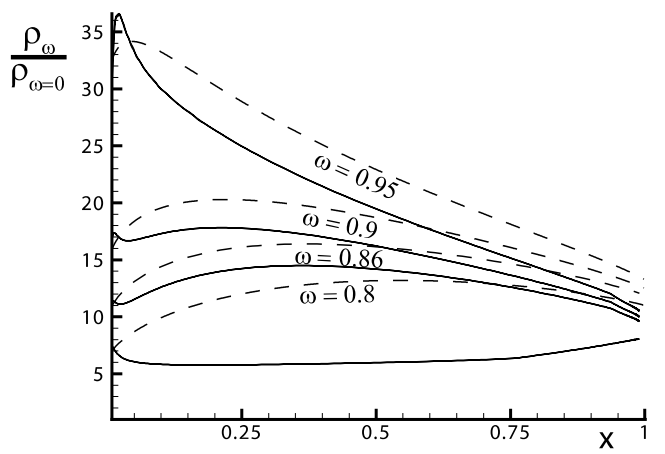

FIG. 9.—Density enhancement of slow wind solutions with rapid rotation rates, $\omega = 0.8$, 0.86, 0.9, and 0.95, relative to a nonrotating wind with the same wind parameters. Dashed curves show analytic results, while solid curves show those obtained from numerical simulations using VH-1.

equatorial mass loss around the cooler, gravity-darkened equator, thus yielding an overall enhancement of the order of 10^2 (Lamers & Pauldrach 1991; Pelupessy et al. 2000). Significantly higher enhancement would require an unrealistically low α to increase further the equatorial mass flux and/or assuming an equatorial surface rotation within a sound speed of the critical (orbital) speed. In the latter case, minor disturbances (e.g., pulsations) in the stellar envelope or photosphere could instead eject material into an orbiting, Keplerian disk (Lee et al. 1991; Owocki 2005), obviating the need to invoke any central role for radiatively driven outflow solutions.

6. SUMMARY AND CONCLUSIONS

Using an analytic approach combined with numerical hydrodynamic simulations, we investigate the reasons for the switch from a steep to shallow acceleration in 1D line-driven stellar wind models as stellar rotation rates are increased beyond a threshold value of $\omega \approx 0.745$. The results indicate that the cause of this switch is the overloading of the base mass-loss rate beyond the point-star CAK value. The latter represents the maximal allowed mass loss for which there can be a *monotonically* accelerating flow speed throughout the entire wind. Furthermore, the finite-disk correction factor (FDCF) reduces the driving effectiveness near the stellar surface and thus reduces the maximal mass loss that can be initiated there. This reduction allows the outer wind to maintain a positive acceleration even as other effects (e.g., centrifugal reduction in effective gravity near the surface) allow for an increase of the base mass loss from its FDCF value.

This problem of wind overloading at large rotation rates was first noticed by Friend & Abbott (1986), who found indeed that beyond some threshold rotation rate, the supercritical, steep-acceleration solutions they were deriving could not be followed beyond some finite radius. The contributions of M. Curé and collaborators have since shown that this termination can be avoided by switching to a shallow-acceleration solution. As rotation increases beyond the threshold value of $\omega \approx 0.745$, the base mass loss becomes greater than the point-star CAK value, and so the only *globally accelerating* solution possible is a shallow one with a subcritical outflow.

However, an important lesson learned from our numerical simulations is that the flow *does not* necessarily follow the solution with a globally monotonic acceleration. We see that the steady 1D solutions for rotating winds actually fall into *four* domains. First, for no or low rotation rates ($\omega < 0.745$), the minimum of the nozzle function is less than unity and occurs at the stellar surface ($x = 0$). This allows the flow to transition to a supercritical outflow directly from the static surface boundary and follow the steep-acceleration solution with a mass-loss rate that is less than the point-star CAK value.

Next, there exits a "gray zone" for rotation rates between $\omega = 0.745$ and $\sim$0.86 where two different solutions are possible. If we restrict ourselves to a strictly positive acceleration, $w' > 0$, then as rotation increases beyond $\omega \approx 0.745$ the base mass loss exceeds the point-star CAK value, and so the only globally accelerating solution possible is one with a shallow acceleration and a mass-loss rate that saturates to the point-star CAK value. On the other hand, if we provide a backup scaling for negative accelerations and investigate cases in which multiple local minima appear in the nozzle function, then overloaded situations in which the square root term in equation (19) becomes negative lead to a "kink" and thus a negative-acceleration or coasting solution. Moreover, for these new kink solutions, the multiple minima of the nozzle function now give rise to mass-loss rates that exceed the point-star CAK value.

This gray zone of kink solutions can be further divided into two domains. For rotation rates between $\omega \approx 0.745$ and $\sim$0.85, the overloading of the wind is not too severe. The coasting solution can thus still reach large distances with a finite speed, so these cases are able to approach a perfectly steady, time-independent state, despite the presence of the discontinuity in slope at the kink. On the other hand, for rotation rates of $\omega = 0.85$, the wind becomes strongly overloaded and eventually stagnates at some finite radius. After enough material has piled up at this radius, it will fall back as a "reaccretion front" toward the star. If the boundary conditions are such that this material is allowed to fall through the lower boundary, then it effectively disappears from the model allowing the simulation to reestablish a wind outflow with a slow-acceleration solution (as in the $\omega = 0.86$ case).

For rotation rates greater than $\omega \approx 0.86$, the global minimum of the nozzle function is unity and occurs at large radii ($x = 1$). In order to satisfy the static surface boundary condition, the flow at all finite radii should be subcritical (but still supersonic), so the only solution possible is the shallow ($-$) acceleration solution, with a mass-loss rate that has saturated to the point-star CAK value.

It is also worth noting that since the nonlinear nature of the flow equations allows more than one solution, slow-acceleration solutions in the $0.75 < \omega < 0.85$ regime are also possible via a change in initial conditions. By initializing the wind using the slow-acceleration steady state found for the $\omega = 0.9$ case, it is possible to achieve final states that do approach the expected slow-acceleration solution (apart from a peculiar upward kink near the outer boundary; see Fig. 8).

One should also add here a few words regarding the validity of the Sobolev approximation for the slow-acceleration solutions. Recall that for the usual case in which the broadening of the line is set by the local ion thermal speed $v_{\rm th}$, the geometric width of the local resonance with the radiation is about a Sobolev length, $l_{\rm Sob} \equiv v_{\rm th}/(dv/dr)$ (Sobolev 1960). Thus, in a supersonic flow, this Sobolev length is of order $v_{\rm th}/v \ll 1$ smaller than a typical flow variation scale, such as the density/velocity scale height $H \equiv |\rho/(d\rho/dr)| \approx v/(dv/dr)$. Therefore, while the flow speeds for the slow-acceleration solutions are lower than those of the steep-acceleration solutions, they are still supersonic throughout nearly the entire wind, so the Sobolev approximation remains quite appropriate.

As noted in § 1, it is important to keep in mind the limited physical relevance of such 1D models. The 2D WCD simulations of Owocki et al. (1994, 1996) and Cranmer & Owocki (1995) serve as an example, showing that for moderately rapid rotation, there can be a 2D flow pattern by which material from higher latitudes is focused toward the equator through the WCD effect. Depending on whether the material reaches the equator above or below some "stagnation point," it either drifts outward or falls back toward the star. This simultaneous infall-plus-outflow behavior is not possible in a steady 1D model but is a perfectly natural occurrence in a 2D simulation. There are also the issues of oblateness, limb darkening, and the nonradial line force and how these affect the latitudinal motion of the flow leading to inhibition of the WCD (Cranmer & Owocki 1995; Owocki et al. 1996; Petrenz & Puls 2000). Finally, equatorial gravity darkening can reduce the wind mass flux from the equator and lead to an equatorial wind density that is lower than near the poles (Owocki et al. 1996). A key point here is that 1D simulations represent a sort of best-case scenario for the formation of a disk. A move to 2D simulations shows that when the relevant physics (such as nonzero, nonradial line forces and gravity darkening) are included, material will tend to be channeled away from the equator and inhibit

disk formation. Thus, if 1D simulations are incapable of producing equatorial densities capable of explaining those inferred in B[e] supergiants, then 2D simulations will most likely not change this.

Beyond even developing a 2D CAK-type model, there remain key physical limitations not accounted for in this CAK formalism. Two examples are the intrinsic, small-scale instability of line driving, and multiple scattering effects. The former might well disrupt a slow-acceleration solution, even though the CAK form of such solutions seems from the present simulations to be a stable attractor. The latter places strict upper limits on the mass flux that can be driven within a geometrically thin disk, since even with ideally tuned line-driving parameters within a CAK model (e.g., choosing an anomalously small CAK exponent α to enhance the expected CAK-type mass-loss rate), radiative driving in the thin disk would generally be limited to one or two scatterings before the photon escapes out of the disk plane (Owocki 2007). Thus, quite generally, radiative driving could not produce a disk outflow that exceeds the single scattering limit. So, to the extent that observational inferences of supergiant B[e] disks imply a very dense medium (dense enough to form dust), it seems more likely that these represent orbiting *Keplerian* disks, with perhaps ablation flows off the disk surface producing the equatorial outflow inferred by observations of Doppler-shifted absorption troughs in UV resonance lines.

We thank M. Curé and R. Nikutta for stimulating our initial interest in this topic. We thank J. Blondin for continuing to make available the VH-1 hydrodynamics code. This work was done with partial support from NSF grants AST 00-97983 and AST 05-07581, NASA *Chandra* grant GO3-3024C, and DFG project FE 573/3-1.

APPENDIX

OUTER CRITICAL POINT LOCATION FOR SHALLOW SOLUTIONS WITH FINITE SOUND SPEED

Let us examine here a key issue regarding the location of the outer critical point for the shallow-acceleration solutions that appear for rotation rates $\omega > 0.75$. For the zero sound-speed limit (as analyzed in §§ 2–3), the radius of this critical point formally approaches infinity, $r_c \rightarrow \infty$, or $x_c \rightarrow 1$ in the scaled inverse radius coordinate $x \equiv 1 - R_*/r$. This raises the issue of whether the numerical hydrodynamic simulations (§§ 4–5) done with a finite outer boundary radius must use some sort of subcritical right boundary condition (with one inward and one outward pointing characteristic), instead of the supercritical outflow boundary conditions (with two outward characteristics) that are usually used in stellar wind simulations.

Note, however, that the hydrodynamic simulations presented above include a small but nonzero sound speed, characterized by the dimensionless parameter $w_s \equiv a^2/v_{\rm esc}^2 \approx 4 \times 10^{-4}$. When this is included in the equation of motion (as in eq. [6]), the additional term on the right-hand side has the scaled form $4w_s/(1-x)$ (we are neglecting the additional w_s/w term on the left-hand side of eq. [6]). The total effective gravity used in the denominator of the nozzle function (see eq. [20]) then takes the form

$$g(x) = 1 - \omega^2(1-x) - \frac{4w_s}{1-x}. \tag{A1}$$

Instead of declining monotonically as x increases, this now has a maximum at some finite radius, which in turn allows the nozzle function to reach a minimum at some finite radius. In a model with a nonzero sound speed, this thus becomes the effective critical point of the slow-acceleration solutions. Since $w_s \ll 1$, this minimum still occurs near $x \lesssim 1$, so to evaluate the location, it is convenient to expand the FDCF about $x = 1$. For a $\beta = 1$ velocity law and $\alpha = \frac{1}{2}$, this gives

$$f(x) \approx 1 + \frac{1-x}{4} \quad \text{for } x \rightarrow 1, \tag{A2}$$

which makes the nozzle function

$$n(x) \equiv \frac{f^2(x)}{g(x)} \approx \frac{1 + (1-x)/2}{1 - \omega^2(1-x) - 4w_s/(1-x)}. \tag{A3}$$

We can easily solve for the critical location x_c through

$$n'(x_c) = 0. \tag{A4}$$

To lowest order in the small parameter $w_s^{1/2} \approx 0.02$, we find

$$x_c \approx 1 - 2\sqrt{\frac{w_s}{\omega^2 + 1/2}} \approx 1 - \frac{0.04}{\sqrt{\omega^2 + 1/2}} \tag{A5}$$

which implies a critical radius of

$$\frac{r_c}{R_*} = 25\sqrt{\omega^2 + 1/2} \tag{A6}$$

The upshot of this is thus that the outer boundary radius used in our numerical models ($R_{\rm max} = 100R_*$) should be well above the critical point ($r_c \lesssim 30.6R_*$) for even the shallow-slope solutions at high rotation rate. Thus, a pure supercritical outflow boundary condition should indeed be appropriate for all the models computed here.

REFERENCES

Abbott, D. C. 1980, ApJ, 242, 1183
Bjorkman, J. E., & Cassinelli, J. P. 1993, ApJ, 409, 429
Castor, J. I., Abbott, D. C., & Klein, R. I. 1975, ApJ, 195, 157 (CAK)
Collela, P., & Woodward, P. R. 1984, J. Comput. Phys., 54, 174
Cranmer, S. R., & Owocki, S. P. 1995, ApJ, 440, 308
———. 1996, ApJ, 462, 469
Curé, M. 2004, ApJ, 614, 929
Curé, M., & Rial, D. F. 2004, A&A, 428, 545
Curé, M., Rial, D. F., & Cidale, L. 2005, A&A, 437, 929
Feldmeier, A., & Nikutta, R. 2006, A&A, 446, 661
Friend, D. B., & Abbott, D. C. 1986, ApJ, 311, 701 (FA86)
Friend, D. B., & MacGregor, K. B. 1984, ApJ, 282, 591
Gayley, K. G. 1995, ApJ, 454, 410
Gayley, K. G., & Owocki, S. P. 2000, ApJ, 537, 461
Holzer, T. E. 1977, J. Geophys. Res., 82, 23
Ignace, R., & Gayley, K. G. 2005, The Nature and Evolution of Disks Around Hot Stars (ASP Conf. Ser. 337; San Francisco: ASP)
Koninx, J. P. M., & Hearn, A. G. 1992, A&A, 263, 208
Kraus, M., & Miroshnichenko, A. S. 2006, Stars with the B[e] Phenomenon (ASP Conf. Ser. 355; San Francisco: ASP)
Lamers, H. J. G. L. M., & Cassinelli, J. 1999, Introduction to Stellar Winds (Cambridge: Cambridge Univ. Press)
Lamers, H. J. G. L. M., & Pauldrach, A. W. A. 1991, A&A, 244, L5
Lee, U., Osaki, Y., & Saio, H. 1991, MNRAS, 250, 432
Owocki, S. 2004, EAS Publ. Ser., 13, 163
———. 2005, in ASP Conf. Ser. 337, The Nature and Evolution of Disks Around Hot Stars, ed. R. Ignace & K. G. Gayley (San Francisco: ASP), 101
———. 2007, in ASP Conf. Ser., Mass Loss from Stars and Evolution of Stellar Clusters, ed. A. de Koter, L. J. Smith, & L. B. F. M. Waters (San Francisco: ASP), in press
Owocki, S. P., Cranmer, S. R., & Blondin, J. M. 1994, ApJ, 424, 887
Owocki, S. P., Cranmer, S. R., & Gayley, K. G. 1996, ApJ, 472, L115
Owocki, S. P., & ud-Doula, A. 2004, ApJ, 600, 1004
Pauldrach, A., & Puls, J. 1990, A&A, 237, 409
Pauldrach, A., Puls, J., & Kudritzki, R. P. 1986, A&A, 164, 86 (PPK86)
Pelupessy, I., Lamers, H. J. G. L. M., & Vink, J. S. 2000, A&A, 359, 695
Pereyra, N. A., Owocki, S. P., Hillier, D. J., & Turnshek, D. A. 2004, ApJ, 608, 454
Petrenz, P., & Puls, J. 2000, A&A, 358, 956
Poe, C. H., & Friend, D. B. 1986, ApJ, 311, 317
Sobolev, V. V. 1960, Soviet Astron., 4, 372
Vink, J. S., de Koter, A., & Lamers, H. J. G. L. M. 1999, A&A, 350, 181
Zickgraf, F.-J., Wolf, B., Stahl, O., Leitherer, C., & Klare, G. 1985, A&A, 143, 421